Insights into the Interaction of Nitrobenzene and the Ag(111) Surface: a DFT Study

Amelia K. Sweet[a] and Sara E. Mason[a,b,*]

[a]Department of Chemistry, University of Iowa, Iowa City IA 52242, USA

[b]Center for Functional Nanomaterials, Brookhaven National Laboratory, Upton NY 11973

***smason@bnl.gov**

Abstract:

This study explores the potential of nitrobenzene as an anolyte material for nonaqueous redox flow batteries (RFBs) by theoretically examining its low-coverage adsorption behavior on neutral and charged Ag(111) model electrode surfaces. At the low coverage limit, DFT calculations show a preference for nitrobenzene to adsorb parallel to the surface, with the benzene ring and nitro group centered over HCP sites. Interactions between nitrobenzene and the surface were analyzed using induced charge density analysis, Bader charge analysis, and projected density of states (PDOS). It was found that nitrobenzene adsorbs primarily through van der waals interactions with the surface. As nitrobenzene accumulates negative charge, the strength of adsorption diminishes. Understanding the electrode-electrolyte interface is crucial for enhancing RFB electrochemical performance, and this study sheds light on nitrobenzene's interaction with a model Ag electrode.

Keywords: Density Functional Theory; Nitrobenzene; Silver; Adsorption; Redox Flow Battery

1. Introduction

The increasing use of intermittent green energy sources such as wind and solar is driving the development of large-scale batteries capable of balancing the fluctuating demands on the power grid [1-3]. Redox flow batteries (RFBs) have emerged as a scalable solution, offering safety benefits in comparison to lithium-ion batteries, and the unique ability to decouple energy and power [4, 5]. In RFBs, energy is stored in redox-active molecules housed in separate tanks. During charging and discharging, these molecules are circulated through the battery, with one undergoing oxidation and the other undergoing reduction. Among RFB types, nonaqueous organic RFBs offer distinct advantages over inorganic and aqueous alternatives.

The use of organic molecules as active redox species (redoxmers) presents an environmentally friendly and easily customizable alternative to metal counterparts [6-8]. Furthermore, nonaqueous solvents offer wider operating voltage windows than water, as well as higher boiling and lower freezing points [9-11]. While extensive research has focused on the development of large, complicated redoxmers, there is growing interest in exploring small organics due to their cost-effectiveness and commercial availability. Nitrobenzene stands out as an attractive option due to its economic viability, stability, and good electrochemical reversibility [12].

A conventional RFB electrolyte typically consists of a solvent, salt, and a redoxmer. The primary function of the solvent is to solvate both the salt and the redoxmer, without directly contributing to the battery's energy density. Liquid electrolytes such as nitrobenzene are appealing because of their inherent liquidity, which reduces solvent requirements [13]. Notable for its role as a precursor to aniline -a valuable compound in industries such as pharmaceuticals, agrochemicals, rubber, and pigments- nitrobenzene has been extensively studied both experimentally and computationally [14, 15].

Several studies have examined the use of nitrobenzene as an anolyte in RFBs. Yu et al. carried out a study pairing nitrobenzene in acetonitrile with iodine in tetraethylene glycol dimethyl ether. At a concentration of 1 M and a current density of 1.0 mA cm^{-2} the authors observed negligible capacity fade over 50 cycles [16]. Subsequently, Liu et al. combined nitrobenzene and several nitrobenzene derivatives with 2,5-di-*tert*-butyl-1-methoxy-4-(20-methoxyethoxy)-benzene (DBMMB) catholyte and reported a capacity retention of 50% over 100 cycles at 50 mM and 40 mA cm^{-2} [17]. Xu et al. also studied nitrobenzene with DBMMD, reporting a capacity retention of 66.1% after 50 cycles at a concentration of 100 mM and a current density of 60 mA cm^{-2} [18]. The impact of solvent on the cycling performance of model nitrobenzene redox flow batteries was studied by Liu et al, who determined that the use of acetonitrile resulted in the highest discharge capacity and a much slower capacity decay compared to systems using other nonaqueous solvents [17]. This indicates that no notable chemical reactions resulting in capacity loss occur between nitrobenzene and acetonitrile in short term experiments. When considering the maximum achievable concentration of nitrobenzene in acetonitrile, Lui et al. and Xu et al. calculate theoretical energy densities of 11892 Wh L^{-1} and 182 Wh L^{-1}, respectively. However, the concentrations used to calculate these values are currently impractical in operational RFBs due to issues such as high viscosity and irreversible dimerization of the nitrobenzene radical anion. Presently, experimental energy densities of the best nonaqueous organic RFBs range from 9.2-22.2 Wh L^{-1} [19] while vanadium RFBs -the most commercially successful- exhibit energy densities ranging from 25-35 Wh L^{-1} [20]. Although vanadium RFBs are more extensively developed, further research holds the potential to make RFBs such as the nitrobenzene battery competitive with vanadium.

Density functional theory (DFT) calculations have been instrumental in understanding various aspects of RFBs and informing design improvements. Xu et al. published DFT results that explore the correlation between singly occupied molecular orbital (SOMO) energies and the stability of radical anions. While molecular DFT is commonly used to study RFB redoxmer properties such as redox potential, and the energy gap and spatial localization of the HOMO/LUMO, periodic DFT for studying the electrode-electrolyte interface in RFBs remains an open-ended area of research [21-24]. Understanding this interface is crucial for developing efficient batteries with long-term stability and can benefit from molecule-surface studies modeled in vacuum conditions [25-34]. Existing literature on RFB electrode-electrolyte interfaces based on vanadium are prolific [35-38].

Beyond vanadium, Howard et. al, investigated the interactions of 2,5-di-tert-butyl-1,4-dimethoxybenzene, benzothiadiazole, acetonitrile, and ethylene carbonate with a model graphene electrode [39]. Ensuring good charge transfer between the electrode and electrolyte is essential for competitive RFB development, underscoring the need for further research in this field.

The inclusion of solvent and charge has a significant effect on the electrochemical environment, as demonstrated by Yuk et al. in their investigation of the catalytic hydrogenation of benzaldehyde over Pt-group metals [40]. Their study assessed the effects of charging the metal surface via the inclusion of additional electrons and modeled solvation effects by incorporating explicit water molecules. We use the charge simulation method described, motivated by its utility for studying the effects of applied potentials. However, due to the substantial difference in size between acetonitrile and water, approximations are necessary when considering solvent. Bramley et al. recently described an approach for calculating the free energy and entropy change of adsorption in the aqueous phase, employing a parametrized solute dielectric cavity, thermodynamic arguments, and DFT calculations with implicit solvation [41]. Singh and Campbell report a method for accurately calculating heats of adsorption for organic molecules on transition metals [42]. Potts et al. highlighted that solvent displacement diminishes the effective adsorption energy of similar molecules such as phenol and benzene, emphasizing the importance of including solvation effects [43]. While employing the methods of Bramley or Singh could offer a more accurate description of solvation effects, they necessitate the use of experimental data that is currently unavailable for our system. In this work, we use the implicit solvation model VASPsol for its cost-effectiveness, simple implementation, and its ability to incorporate an implicit electrolyte-based countercharge when evaluating charged surfaces [44,45]. The countercharge distribution of VASPsol offers a more precise representation of the electrochemical double layer compared to the commonly used homogeneous background method. Additionally, good agreement has been shown between experimental solvation energies and solvation energies calculated using VASPsol [44]. Therefore, as a preliminary step for future investigations, we adopt a more simplified approach to solvation using VASPsol, as recently applied by Wong et al. in their examination of nitrobenzene reduction on transition metals [34].

In this study, our goal is to enhance the understanding of the electrochemical environment within a nitrobenzene RFB. We employ periodic DFT to examine the adsorption of nitrobenzene onto both neutral and charged Ag(111) electrode surfaces in an acetonitrile solvent environment, which is modeled at the continuum dielectric level. Our investigation of the charged surface seeks to clarify how nitrobenzene interacts with the Ag surface under the reducing conditions observed at an RFB anode. We chose silver, motivated by its cost-effectiveness compared to other noble metals, and the (111) surface is selected for its thermodynamic stability [46]. Furthermore, we include acetonitrile solvent, modeled implicitly, in our calculations, chosen for its wide electrochemical window and its ability to solvate nitrobenzene effectively, with the aim of better representing the electrochemical environment in an RFB [47].

2. Computational Details

DFT calculations were performed using the Vienna Ab Initio Simulation Package (VASP) and the PBE-GGA exchange-correlation functional [48-52]. Calculations comparing exchange-correlation functionals were carried out and are reported in table S1. The DFT-D3 method of Grimme with zero-damping function was used to account for van der waals interactions [53]. Projector augmented-wave (PAW) pseudopotentials were used with a converged planewave cutoff of 450 eV [54]. Gaussian smearing was employed with a width of 0.1 eV. A 4x4 supercell four atomic layers thick was used to model the Ag(111) surface, with a DFT optimized lattice constant of 4.14 Å. To ensure that a 4x4 supercell was sufficiently large to achieve isolated adsorption, adsorption for a single 5x5 cell was carried out. The adsorption energies –presented in table S2- are the same for both supercells. 20 Å of vacuum was included between slabs to prevent unwanted interactions between periodic images. A 6x6x1 Monkhorst-Pack k-point grid was used [55]. All atoms were allowed to relax during geometry optimizations, with a force convergence criterion of 0.03 eV/Å and an electronic convergence criterion of 1×10^{-6} eV. Isolated nitrobenzene was modeled in a 20x20x20 Å box to prevent interaction of periodic repeats, and only the gamma point was sampled. Benzene exhibits adsorption to the Ag(111) surface in eight high-symmetry configurations. As described by Saeys et al, benzene can adsorb at bridge, top, HCP and FCC sites and can be rotated by 30° at each of these sites [56]. At four of the eight configurations the nitro group can be situated over two distinct sites depending on the carbon to which it is attached. To account for this variability, the position of the nitro group is specified by a subscript at the end of each configuration's name. The initial adsorption geometries are shown in Figure 1c, and the bare Ag slab is shown in 1a and 1b.

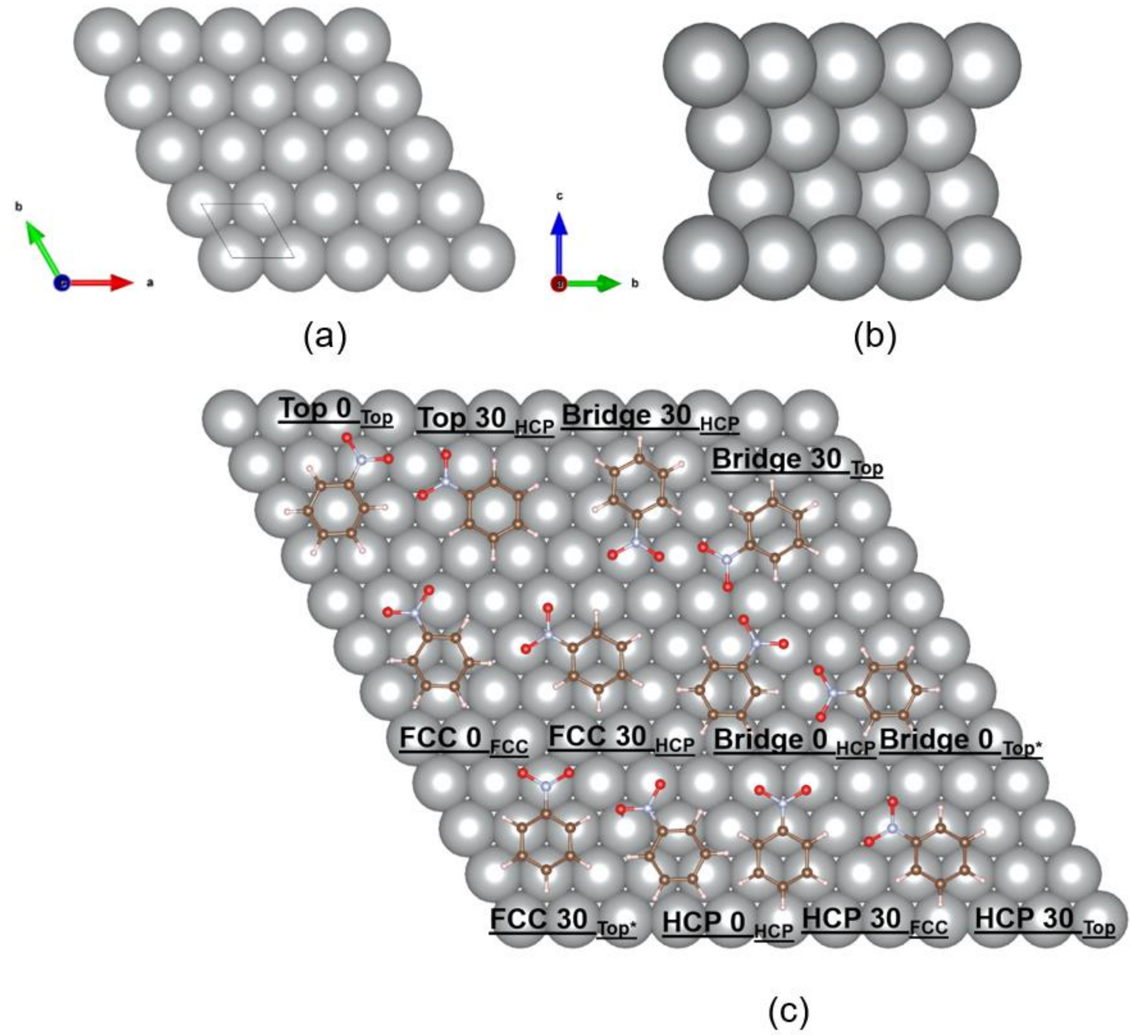
(a) (b) (c)

Figure 1. Top (a) and side (b) views of the 4x4 Ag (111) supercell and adsorption sites of nitrobenzene on the Ag(111) surface (c). Red, blue, brown, white and gray spheres represent oxygen, nitrogen, carbon, hydrogen and silver atoms, respectively.

The adsorption energy (E_{chem}) was calculated using the definition $E_{chem} = E_{Ag/NB} - E_{Ag} - E_{NB}$, where $E_{Ag/NB}$, E_{Ag}, and E_{NB} are the total energies of the Ag-slab with nitrobenzene, Ag-slab, and isolated nitrobenzene, respectively. Acetonitrile solvent was modeled using the VASPsol implicit solvation model with a dielectric constant (ε) of 37.5, and the Debye length was set to 9.61 Å. Crystallographic figures were generated using the VESTA software [57]. The Bader program of the Henkleman group was used to calculate electronic charges on atoms [58-61]. Bader charges were visualized using OVITO [62]. VASPKIT was used to process the density of states data [63]. Charged calculations were performed by adding electrons to the system using the NELECT parameter. The number of additional electrons is denoted as Q. In this work, Q = 1-4 is studied. A background charge was included via VASPsol to ensure neutrality of the system. The adsorption energy of the charged structures (E_{chem}) was calculated using the definition E_{chem} =

$E_{Ag/NB + Ne} - E_{Ag + Ne} - E_{NB}$, where $E_{Ag/NB}$, E_{Ag}, and E_{NB} are the total energies of the Ag-slab with nitrobenzene, Ag-slab, and isolated nitrobenzene, respectively and Ne denotes the number of electrons added to the structure. On charged surfaces, adsorption energies are linearly proportional to the inverse of the vacuum spacing between slabs (1/L) due to coulomb interactions. To correct for this error, adsorption energies were calculated using vacuum spacings of 20, 30, 40, 50, and 60 Å and the results were extrapolated to the infinite vacuum ($L \rightarrow \infty$) [64]. The geometry of the 20 Å structures was used to construct the 30, 40, 50, and 60 Å structures. Single point energies of the 30-60 Å structures were calculated and used to determine adsorption energies due to the cost of full geometry optimizations.

3. Results & Discussion

The DFT calculated values of E_{chem} are presented in Table 1. For the twelve unique optimized structures, the range in values of E_{chem} is 0.16 eV, indicating a relatively flat potential energy surface for nitrobenzene over the surface. Values cluster based on the adsorption sites, with the preferred adsorbed geometries exhibiting the benzene ring and the nitro group centered over HCP and FCC sites. The nitro group exhibited a stronger correlation with site preference than the benzene ring, indicating the functional group plays a greater role in adsorption. In the configurations denoted with asterisks, the nitro group was initially placed over a top site but shifted to a hollow HCP site upon optimization. Configurations in which the benzene ring and/or the nitro group are centered over HCP sites have adsorption energies ranging from -0.89 to -0.99 eV, whereas for top sites that did not optimize to HCP sites the range is -0.83 to -0.92 eV. The HCP site preference is consistent with DFT calculations reported by Miller et al.[33] Images of all optimized structures are shown in Figures S1-12 in the supporting information. Adsorption energies for each structure were calculated without dispersion corrections to assess the degree to which van der waals (vdW) interactions contribute to the strength of adsorption. Table S3 shows that adsorption energies in the absence of dispersion corrections range from –0.09 eV to 0.03 eV, indicating that nitrobenzene adsorbs to the Ag(111) surface primarily through physisorption.

Table 1

Calculated values of E_{chem} (eV) and bond distances, d, (Å) of modeled configurations of nitrobenzene on Ag(111). Atoms labels are displayed graphically in figure 2c.

Configuration	E_{chem}	d (N-O)	d (C-N)	d (C1-C2)	d (C2-C3)	d (C3-C4)
Isolated nitrobenzene in implicit solvent	N/A	1.244	1.468	1.400	1.394	1.397
HCP 0^o $_{HCP}$	-0.99	1.279	1.421	1.402	1.397	1.409
Bridge 0° $_{Top}$*	-0.99	1.278	1.424	1.402	1.396	1.409
FCC 30° $_{Top}$*	-0.99	1.276	1.424	1.402	1.396	1.408
HCP 30° $_{FCC}$	-0.98	1.276	1.428	1.402	1.396	1.408

FCC 30° $_{\text{HCP}}$	-0.98	1.270	1.434	1.402	1.396	1.406
FCC 0° $_{\text{FCC}}$	-0.98	1.277	1.423	1.403	1.397	1.409
Bridge 30° $_{\text{HCP}}$	-0.97	1.272	1.431	1.402	1.396	1.408
Bridge 0° $_{\text{HCP}}$	-0.95	1.272	1.428	1.403	1.398	1.408
Top 30° $_{\text{HCP}}$	-0.92	1.276	1.426	1.401	1.395	1.406
HCP 30° $_{\text{Top}}$	-0.89	1.260	1.441	1.403	1.397	1.404
Bridge 30° $_{\text{Top}}$	-0.88	1.258	1.446	1.402	1.397	1.404
Top 0° $_{\text{Top}}$	-0.83	1.255	1.451	1.401	1.396	1.403

* The naming is based on the initial geometry of the adsorption configuration. In these configurations, nitrobenzene optimizes to a different position, as shown in figures S1-12.

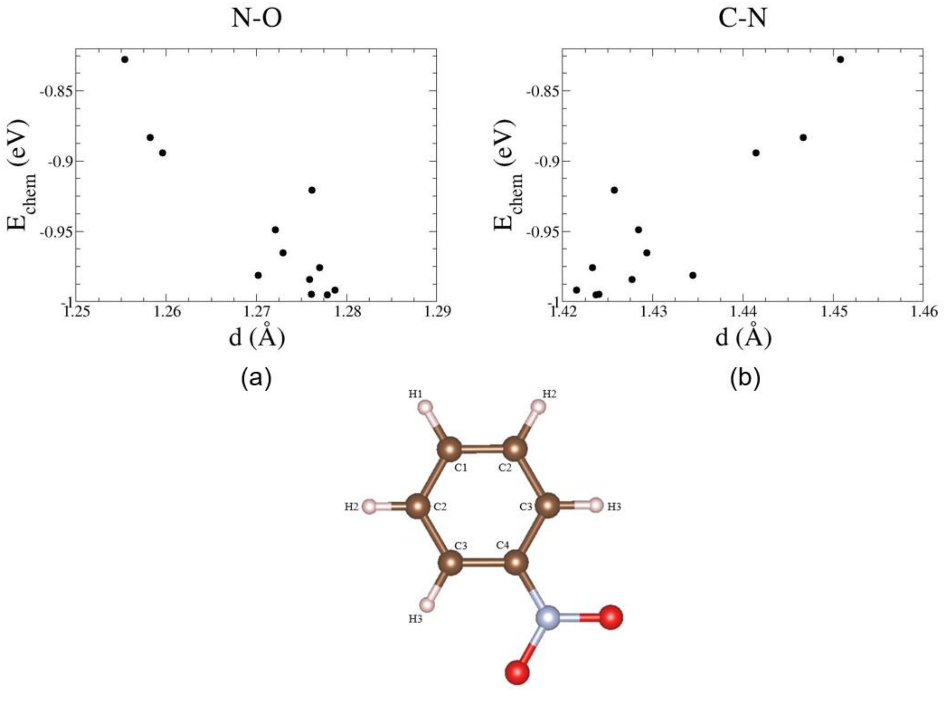

(a)

(b)

(c)

Figure 2. Plots of E_{chem} as a function of N-O (a) and C-N (b) bond lengths of adsorbed nitrobenzene. Each configuration in table 1 is represented by a point on each of the graphs. The numerical labeling of the atoms of nitrobenzene is presented in (c). Red, blue, brown, and white spheres represent oxygen, nitrogen, carbon, and hydrogen atoms, respectively.

Also reported in Table 1 are key aspects of the optimized geometries for nitrobenzene on the Ag(111) surface. Compared to the isolated molecule, all adsorption geometries show a contraction of the C-N bond and an elongation of the N-O bond. Adsorption-induced changes in bond distances correlate with values of E_{chem}, as shown in Figure 2. For example, the HCP $0^o{}_{HCP}$ and Top $0°{}_{Top}$ structures have E_{chem} values and C-N bond distances of –0.99 eV and 1.421 Å, and –0.83 eV and 1.451 Å, respectively.

Molecular-level details of the adsorption mechanism can be informed by the adsorption-induced changes in charge density [65], $\Delta\rho$, defined as $\Delta\rho = \rho Ag/NB - \rho Ag - \rho NB$ where $\rho_{Ag/NB}$, ρ_{Ag}, and ρ_{NB} are the charge density of the Ag-slab with nitrobenzene, Ag-slab, and isolated nitrobenzene, respectively. For this visual analysis, the latter two quantities are calculated for the respective components in the exact same geometry as in the chemisorbed system. To guide the interpretation of $\Delta\rho$ it is useful to visualize the electronic structure of the isolated nitrobenzene molecule. Figure 3 shows the HOMO and LUMO of nitrobenzene solvated in implicit acetonitrile. The LUMO has a bonding orbital along the C-N bond and antibonding orbitals along the N-O bonds.

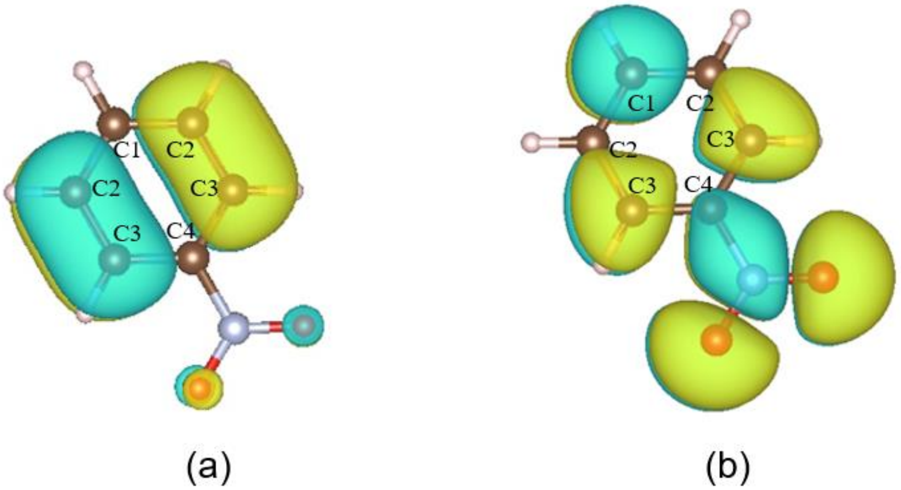

Figure 3. HOMO (left) and LUMO (right) of nitrobenzene. Red, blue, brown, and white spheres represent oxygen, nitrogen, carbon, and hydrogen atoms, respectively. The yellow and blue regions indicate phase.

The adsorption-induced C-N contraction and N-O elongation (Table 1) and the bonding/antibonding characteristics of the nitrobenzene LUMO suggest that the molecule-surface interaction involves electron donation from the Ag surface into the LUMO of nitrobenzene. To confirm and visualize this, we calculate $\Delta\rho$ for the HCP-$0^o{}_{HCP}$ configuration, which exhibits the most favorable value of E_{chem}. Isosurfaces of $\Delta\rho$ are shown in Figure 4, where charge gain and charge loss are shown in yellow and blue, respectively.

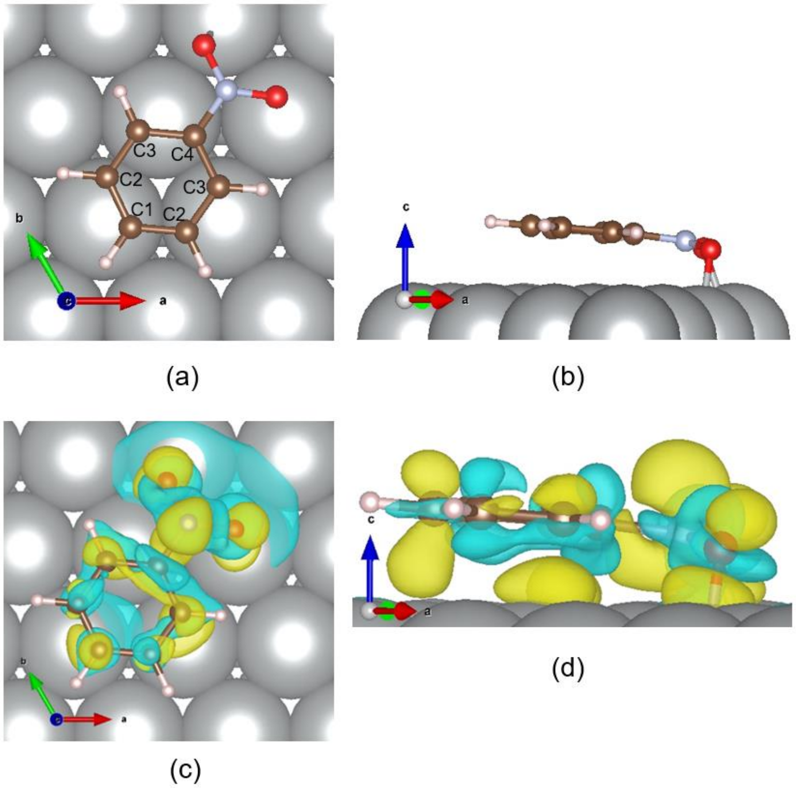

(a) (b)

(c) (d)

Figure 4. Top (a) and side (b) views of the HCP-0º $_{\mathrm{HCP}}$ configuration. Top (c) and side (d) views of charge density difference plots of adsorbed nitrobenzene on the Ag(111) surface in the HCP-0º $_{\mathrm{HCP}}$ configuration, where the yellow and blue regions denote charge gain and charge loss arising from the adsorption process, respectively. The isosurface value is $6.3\text{x}10^{-4}$ Å^{-3}.

The interpretation of $\Delta\rho$ suggests that the nitro group and regions around the C1 and C3 carbon atoms experience an increase in electron density upon adsorption, indicating partial occupancy of the LUMO from surface charge transfer. Conversely, regions surrounding the C4 and the C2 carbons display a decrease in electron density. Notably, the shape of $\Delta\rho$ isosurfaces for electron density gain (yellow) near the oxygen atoms and the C1 atom resemble atomic p orbitals and are directed along the surface normal, indicative of p-d hybridization with the surface.

The adsorption mechanism is further probed through Bader charge analysis, focusing on the most and least favorable configurations (HCP-0º $_{\mathrm{HCP}}$ and Top 0° $_{\mathrm{Top}}$ with Echem values of –0.99 end –0.83 eV, respectively). The change in Bader charges resulting from adsorption (Δq) were calculated using the equation $\Delta q = q_{\mathrm{Ag/NB}} - q_{\mathrm{Ag}} - q_{\mathrm{NB}}$ where q has units of fundamental electric charge and $q_{\mathrm{Ag/NB}}$, q_{Ag}, and q_{NB} are the Bader charges of the Ag-slab with nitrobenzene, Ag-slab, and isolated nitrobenzene, respectively.

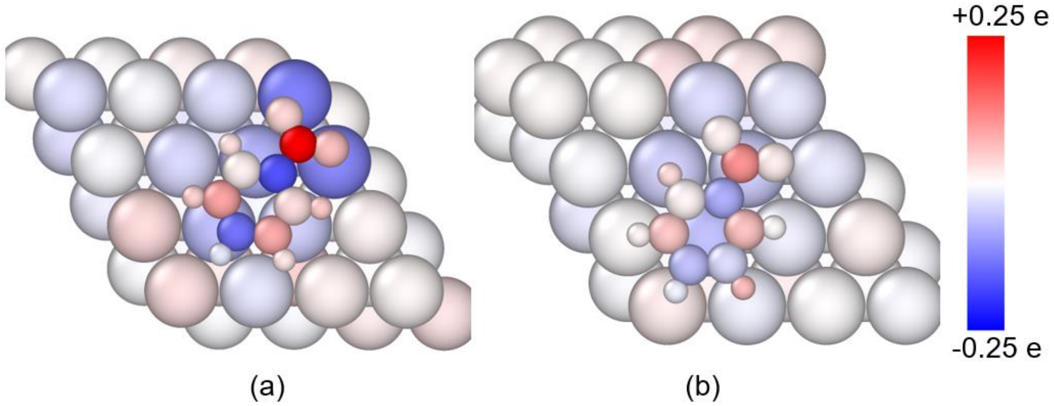

Figure 5. Δq of the HCP-0º $_{HCP}$ (a) and Top 0° $_{Top}$ (b) configurations. Red and blue indicate an increase and decrease in charge, respectively, as indicated by the color scale.

Δq is visualized in Figure 5. As shown by the Δq gradients, the adsorption-induced charge transfer is localized around the nitro group, as was interpreted from the Δρ plots (Figure 4). Specifically, the C4 atom adjacent to N shows a notable decrease in charge. Away from the nitro group, Δq values are smaller in magnitude. In comparing the two adsorption configurations, a larger range of Δq is seen for HCP-0º $_{HCP}$ (E_{chem} = -0.99 eV) relative to Top 0° $_{Top}$ (E_{chem} = -0.83 eV). As expected, the Ag atoms proximal to nitrobenzene show more significant changes in Bader charge than the atoms further from molecule, with the Ag atoms beneath the nitro group showing a loss in electronic charge. Table S4 in the supporting information reports Δq values for all configurations.

Atom projected density of states (PDOS) was used to confirm the p-d hybridization between the p orbitals of O and the d orbitals of the silver surface suggested by the Δρ diagrams and Bader charge analysis. Hybridization can be inferred from PDOS by the presence of intense peaks at common energies for projections onto different atomic states. In Figure 6, we plot the Ag d PDOS of the bare Ag(111) surface (left) and the O p of the free nitrobenzene (right). The central panel shows the adsorbed system with the oxygen p and Ag d PDOS plotted together. The three panels shown in Figure 6 can be interpreted like an orbital energy diagram, with the isolated states on either side and those of the adsorbed system in the middle. In the adsorbed system, it can be seen that the oxygen p orbitals mix with the Ag d orbitals following adsorption, as evidenced in figure 6 by the change in energy of oxygen atom p states to align with the silver d band. Using the orbital interaction categorization of Hoffmann, the PDOS shows that there is a two orbital stabilizing interaction, where the surface acts as an electron donor and the nitrobenzene as an acceptor [65]. Additionally, the LUMO downshifts in energy to straddle to fermi level. This is consistent with the electron transfer to the LUMO seen in the Bader charge analysis and induced charge density analysis. In an RFB, this p-d hybridization and the downshifting of the LUMO should facilitate electron transfer across the interface.

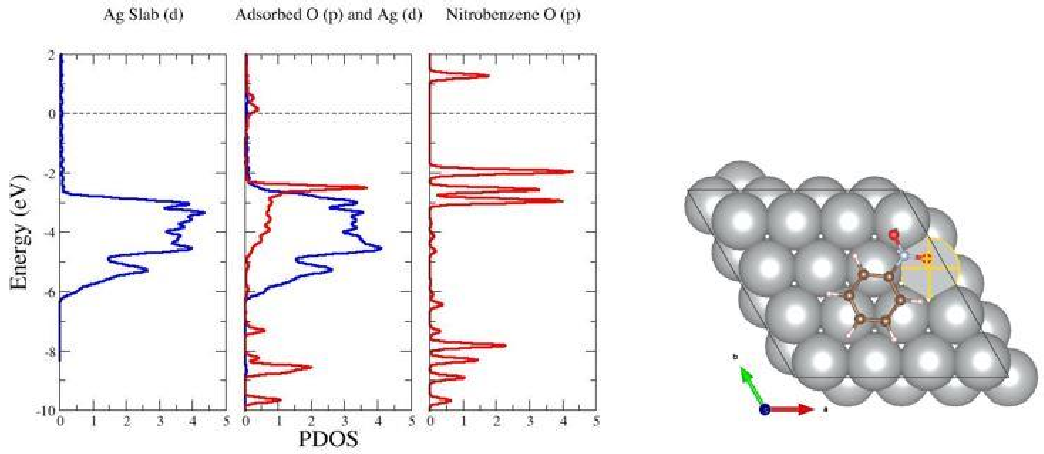

(a)

(b)

Figure 6. PDOS (arbitrary intensity) of the d orbitals of Ag atoms and the p orbitals of O atoms with the fermi level referenced to 0 eV (a). Since molecules do not have well-defined fermi levels, the O 1s levels of the free and adsorbed oxygen atom of nitrobenzene were compared to ensure that nitrobenzene's PDOS panel was correctly aligned with the adsorbed molecule's PDOS. Nitrobenzene's PDOS plot was downshifted by 1.42 eV to correctly align the nonbonding 1s orbitals. The Ag and O atoms selected in the PDOS analysis are highlighted (b).

Having detailed the adsorption mechanism through electronic structure analysis, our next objective is to examine how small perturbations to the system influence the adsorption process. Motivated by RFB function, we explore how the charge state of the molecule influences interactions with the surface. This was studied by adding electronic charge (in integer values, denoted Q, from 1-4) to the system [67, 68]. The overall calculation retains charge neutrality through the screening charges provided by the polarizable continuum solvent model. The same initial adsorption geometries were used to carry out DFT geometry optimizations at Q = 1, and the total energies of the optimized structures were used to calculate values of E_{chem}, presented in table S5. Images of the optimized structures are shown in figures S13-24. Before correcting for coulomb interactions, values of E_{chem} range from -0.79 to –0.97 eV, slightly lower than for the neutral structures (0.83-0.99 eV). Applying the shift in energy calculated for the Q=1 HCP-0^{o} $_{HCP}$ configuration due to long-range Coulomb interactions to all the structures, the adsorption energies range from –0.92 to –0.74. Similar to the neutral adsorption system, HCP sites are the most stable adsorption sites and top sites are the least stable.

Having determined that the HCP-0º $_{HCP}$ configuration remains preferred at Q = 1, we carry out and compare charge density analysis using Bader charges for this structure at values of Q ranging from 0 to 4. Figure 7 shows how the extra electrons are distributed by mapping Bader charges onto the structure.

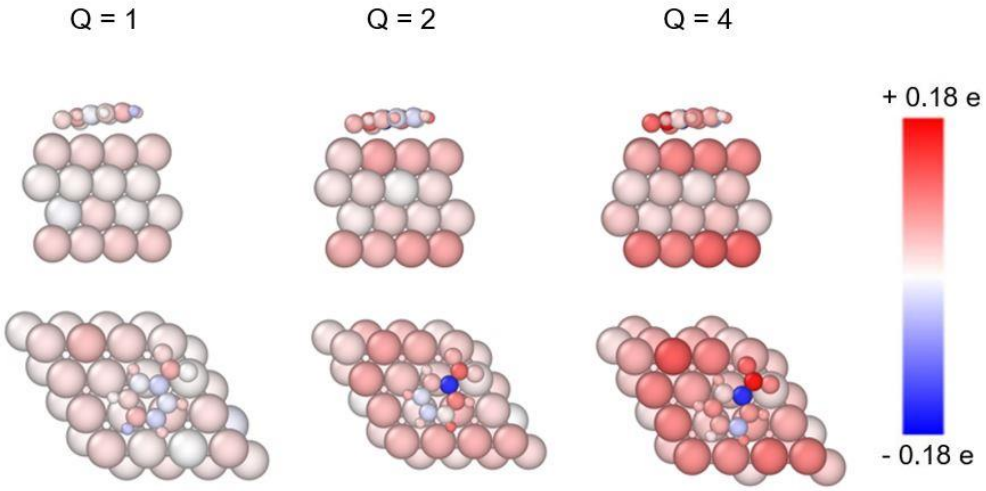

Figure 7. Difference in the Bader charges of the HCP-0º $_{HCP}$ configurations at Q = 1, 2, and 4 and the same structure at Q = 0. Red and blue indicate an increase and decrease in charge, respectively, as indicated by the color scale.

Upon adsorption, the additional electronic charge is distributed over the nitrobenzene-Ag(111) system, including many subtle changes to individual Ag atoms. To track the charge state of the adsorbate we define Σq, the sum of the individual Bader charges over all the atoms in the adsorbed nitrobenzene. We calculate this value as a difference relative to the Q = 0 total and denote this as ΔΣq, reported in Table 2. Adsorption energies obtained using the Poisson-Boltzmann countercharge distribution (table 2) were compared to those obtained using the homogenous countercharge method, with results presented in table S6. The plots used to extrapolate the adsorption energies to the infinite vacuum are presented in figure S25.

Table 2

Calculated values of E_{chem}, (eV), sum of Bader charges relative to Q = 0 for the adsorbed nitrobenzene, ΔΣq (e), and key bond distances, d, (Å) of the HCP-0º $_{HCP}$ configuration at Q = 0, 1, 2, and 4.

Q	**E_{chem}**	**ΔΣq**	**d (O-Ag)**	**d (N-O)**	**d (C-N)**	**d (C3-C4)**

0	-0.99	N/A	2.506	1.279	1.421	1.409
1	-0.90	0.18	2.521	1.288	1.411	1.412
2	-0.84	0.42	2.527	1.300	1.397	1.417
4	-0.85	0.88	2.842	1.312	1.372	1.428

As Q increases, contraction of the C-N bond and elongation of the N-O and C3-C4 bonds result. Our interpretation of this result is that the excess electrons of nitrobenzene at $Q > 0$ occupy the LUMO, causing the bond length changes. O-Ag bond distances show that nitrobenzene moves further from the surface and adsorbs less strongly at higher values of Q, as seen in Figure 8.

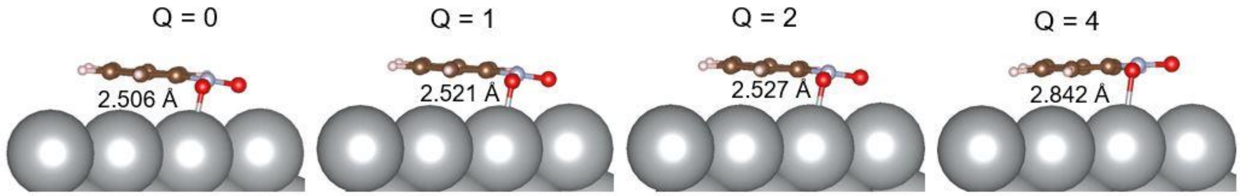

Figure 8. Adsorption geometries of the HCP-0° $_{\mathrm{HCP}}$ configuration at Q = 0, 1, 2, and 4. The displayed bond distances indicate the distance between the oxygen and silver atoms connected via the depicted bond.

By monitoring the behavior of nitrobenzene adsorption as a function of charge, we infer that as the molecule forms a radical anion, it starts to desorb from the electrode. This would be desirable behavior in an RFB, where the desorption of charged species makes room at the electrode surface for neutral molecules to undergo reduction.

4. Conclusions

This study aimed to investigate the adsorption behavior of nitrobenzene on the Ag(111) surface using DFT calculations. Results showed that at low coverage, the molecule adsorbs parallel to the surface with the benzene ring and the nitro group centered over HCP and FCC sites. Various charge density analyses were conducted to elucidate the adsorption mechanism. $\Delta\rho$ diagrams suggest p-d hybridization between the O atoms of nitrobenzene and the d orbitals of the Ag surface, which was supported by Bader charge and PDOS analysis. Changes in bond length and charge distribution were attributed to adsorption-induced charge transfer from the Ag surface to the LUMO of nitrobenzene. By modeling the system with excess electron charge denstiy, evidence of additional charge transfer to the LUMO was seen, ultimately leading to desorption. The adsorption of neutral nitrobenzene and desorption of charged nitrobenzene present potential benefits for RFBs. Coverage-dependant adsorption of nitrobenzene to the Ag(111) surface will be the subject of a subsequent study with accompanying experimental data.

Acknoweldgements

AKS acknowledges funding support provided by the National Science Foundation (NSF) under Cooperative Agreement Number 2019574. This work used the Theory and Computation facility of the Center for Functional Nanomaterials (CFN), which is a U.S. Department of Energy Office of Science User Facility, at Brookhaven National Laboratory under Contract No. DE-SC0012704. Computational support was provided in part by the University of Iowa.

Author Contributions

A.K.S.: Conceptualization, Formal analysis, Investigation, Visualization, Writing – original draft, Writing – review and editing S.E.M.: Conceptualization, Resources, Supervision, Funding acquisition, Writing- original draft, Writing – review and editing, Project administration

Citations

[1] Dunn, B.; Kamath, H.; Tarascon, J.-M. Electrical Energy Storage for the Grid: A Battery of Choices. *Science* **2011**, *334* (6058), 928-935. DOI: 10.1126/science.1212741.

[2] Yang, Z.; Zhang, J.; Kintner-Meyer, M. C. W.; Lu, X.; Choi, D.; Lemmon, J. P.; Liu, J. Electrochemical Energy Storage for Green Grid. *Chemical Reviews* **2011**, *111* (5), 3577-3613. DOI: 10.1021/cr100290v.

[3] Soloveichik, G. L. Flow Batteries: Current Status and Trends. *Chemical Reviews* **2015**, *115* (20), 11533-11558. DOI: 10.1021/cr500720t.

[4] Arévalo-Cid, P.; Dias, P.; Mendes, A.; Azevedo, J. Redox flow batteries: a new frontier on energy storage. *Sustainable Energy & Fuels* **2021**, *5* (21), 5366-5419. DOI: 10.1039/d1se00839k.

[5] Leung, P.; Li, X.; Ponce de León, C.; Berlouis, L.; Low, C. T. J.; Walsh, F. C. Progress in redox flow batteries, remaining challenges and their applications in energy storage. *RSC Advances* **2012**, *2* (27). DOI: 10.1039/c2ra21342g.

[6] Chen, H.; Cong, G.; Lu, Y.-C. Recent progress in organic redox flow batteries: Active materials, electrolytes and membranes. *Journal of Energy Chemistry* **2018**, *27* (5), 1304-1325. DOI: 10.1016/j.jechem.2018.02.009.

[7] Wei, X.; Pan, W.; Duan, W.; Hollas, A.; Yang, Z.; Li, B.; Nie, Z.; Liu, J.; Reed, D.; Wang, W.; et al. Materials and Systems for Organic Redox Flow Batteries: Status and Challenges. *ACS Energy Letters* **2017**, *2* (9), 2187-2204. DOI: 10.1021/acsenergylett.7b00650.

[8] Fischer, P.; Mazúr, P.; Krakowiak, J. Family Tree for Aqueous Organic Redox Couples for Redox Flow Battery Electrolytes: A Conceptual Review. *Molecules* **2022**, *27*, 560. DOI: 10.3390/molecules27020560.

[9] Ding, Y.; Zhang, C.; Zhang, L.; Zhou, Y.; Yu, G. Molecular engineering of organic electroactive materials for redox flow batteries. *Chemical Society Reviews* **2018**, *47* (1), 69-103. DOI: 10.1039/c7cs00569e.

[10] Gong, K.; Fang, Q.; Gu, S.; Li, S. F. Y.; Yan, Y. Nonaqueous redox-flow batteries: organic solvents, supporting electrolytes, and redox pairs. *Energy & Environmental Science* **2015**, *8* (12), 3515-3530. DOI: 10.1039/c5ee02341f.

[11] Li, M.; Rhodes, Z.; Cabrera-Pardo, J. R.; Minteer, S. D. Recent advancements in rational design of non-aqueous organic redox flow batteries. *Sustainable Energy & Fuels* **2020**, *4* (9), 4370-4389. DOI: 10.1039/d0se00800a.

[12] Ramar, A.; Wang, F.-M.; Foeng, R.; Hsing, R. Organic redox flow battery: Are organic redox materials suited to aqueous solvents or organic solvents? *Journal of Power Sources* **2023**, *558*. DOI: 10.1016/j.jpowsour.2022.232611.

[13] Robertson, L. A.; Afsar Uddin, M.; Shkrob, I. A.; Moore, J. S.; Zhang, L. Liquid Redoxmers for Nonaqueous Redox Flow Batteries. *ChemSusChem* **2023**, *16* (14). DOI: 10.1002/cssc.202300043.

[14] Rappoport, Z. The Chemistry of Anilines, Part 1; 2007.

[15] Roger A Sheldon, H. v. B. Fine Chemicals Through Heterogeneous Catalysis; 2000. DOI: 10.1002/9783527612963.

[16] Yu, X.; Yu, W. A.; Manthiram, A. A mediator-ion nitrobenzene - iodine nonaqueous redox flow battery with asymmetric solvents. *Energy Storage Materials* **2020**, *29*, 266-272. DOI: 10.1016/j.ensm.2020.04.023.

[17] Liu, B.; Tang, C. W.; Zhang, C.; Jia, G.; Zhao, T. Cost-Effective, High-Energy-Density, Nonaqueous Nitrobenzene Organic Redox Flow Battery. *Chemistry of Materials* **2021**, *33* (3), 978-986. DOI: 10.1021/acs.chemmater.0c04118.

[18] Xu, D.; Zhang, C.; Zhen, Y.; Li, Y. Liquid Nitrobenzene-Based Anolyte Materials for High-Current and -Energy-Density Nonaqueous Redox Flow Batteries. *ACS Appl Mater Interfaces* **2021**, *13* (30), 35579-35584. DOI: 10.1021/acsami.1c05564.

[19] Yan Y.; Sitaula P.; Odom SA.; Vaid TP. High Energy Density, Asymmetric, Nonaqueous Redox Flow Batteries without a Supporting Electrolyte. *ACS Appl Mater Interfaces* **2022**, 14 (44), 49633-49640. DOI: 10.1021/acsami.2c10072.

[20] Sánchez-Díez, E.; Ventosa, E.; Guarnieri, M.; Trovò, A.; Flox, C.; Marcilla, R.; Soavi, F.; Mazur, P.; Aranzabe, E.; Ferret, R. Redox Flow Batteries: Status and Perspective towards Sustainable Stationary Energy Storage. *Journal of Power Sources* **2021**, *481*, 228804, DOI: 10.1016/j.jpowsour.2020.228804.

[21] Duke, R.; Bhat, V.; Risko, C. Data storage architectures to accelerate chemical discovery: data accessibility for individual laboratories and the community. *Chem Sci* **2022**, 13 (46), 13646-13656. DOI: 10.1039/d2sc05142g.

[22] Pahlevaninezhad, M.; Leung, P.; Velasco, P. Q.; Pahlevani, M.; Walsh, F. C.; Roberts, E. P. L.; Ponce de León, C. A nonaqueous organic redox flow battery using multi-electron quinone molecules. *Journal of Power Sources* **2021**, 500. DOI: 10.1016/j.jpowsour.2021.229942.

[23] Park, J.; Lee, Y.; Yun, D.; Kim, D.; Hwang, G.; Han, B.; Kim, Y.; Jung, J.; Jeon, J. A benzo[a]phenazine-based redox species with highly reversible two-electron reaction for aqueous organic redox flow batteries. *Electrochimica Acta* **2023**, 439. DOI: 10.1016/j.electacta.2022.141644.

[24] Huang, M.; Hu, S.; Yuan, X.; Huang, J.; Li, W.; Xiang, Z.; Fu, Z.; Liang, Z. Five-Membered-Heterocycle Bridged Viologen with High Voltage and Superior Stability for Flow Battery. *Advanced Functional Materials* **2022**, *32* (16). DOI: 10.1002/adfm.202111744.

[25] Mahata, A.; Rai, R. K.; Choudhuri, I.; Singh, S. K.; Pathak, B. Direct vs. indirect pathway for nitrobenzene reduction reaction on a Ni catalyst surface: a density functional study. *Phys Chem Chem Phys* **2014**, *16* (47), 26365-26374. DOI: 10.1039/c4cp04355c.

[26] Miller, D. P.; Simpson, S.; Tyminska, N.; Zurek, E. Benzene derivatives adsorbed to the Ag (111) surface: Binding sites and electronic structure. *J Chem Phys* **2015**, *142* (10), 101924. DOI: 10.1063/1.4908267.

[27] Sheng, T.; Qi, Y.-J.; Lin, X.; Hu, P.; Sun, S.-G.; Lin, W.-F. Insights into the mechanism of nitrobenzene reduction to aniline over Pt catalyst and the significance of the adsorption of phenyl group on kinetics. *Chemical Engineering Journal* **2016**, *293*, 337-344. DOI: 10.1016/j.cej.2016.02.066.

[28] Zhang, L.; Cao, X.-M.; Hu, P. Insight into chemoselectivity of nitroarene hydrogenation: A DFT-D3 study of nitroarene adsorption on metal surfaces under the realistic reaction conditions. *Applied Surface Science* **2017**, *392*, 456-471. DOI: 10.1016/j.apsusc.2016.09.031.

[29] Zhang, L.; Jiang, J.; Shi, W.; Xia, S.; Ni, Z.; Xiao, X. Insights into the hydrogenation mechanism of nitrobenzene to aniline on Pd3/Pt(111): a density functional theory study. *RSC Advances* **2015**, *5* (43), 34319-34326. DOI: 10.1039/c5ra02389k.

[30] Millán, R.; Boronat, M. Hydrogenation of substituted nitroaromatics on non-noble metal catalysts: mechanistic insights to improve selectivity. *Faraday Discuss* **2021**, *229*, 297-317. DOI: 10.1039/c9fd00126c.

[31] Millán, R.; Liu, L.; Boronat, M.; Corma, A. A new molecular pathway allows the chemoselective reduction of nitroaromatics on non-noble metal catalysts. *Journal of Catalysis* **2018**, 364, 19-30. DOI: 10.1016/j.jcat.2018.05.004.

[32] Hajiahmadi, Z.; Tavangar, Z. Investigating the adsorption of nitrobenzene on M/Pd (1 1 1) bimetallic surface as an effective catalyst. *Applied Surface Science* **2018**, *454*, 343-349. DOI: 10.1016/j.apsusc.2018.05.117.

[33] Zhang, L.; Shao, Z.-J.; Cao, X.-M.; Hu, P. Insights into Different Products of Nitrosobenzene and Nitrobenzene Hydrogenation on Pd(111) under Realistic Reaction Conditions. *The Journal of Physical Chemistry C* **2018**, *122* (35). DOI: 10.1021/acs.jpcc.8b05364.

[34] Wong, A. J.-W.; Miller, J. L.; Janik, M. J. Elementary mechanism for the electrocatalytic reduction of nitrobenzene on late-transition-metal surfaces from density functional theory. *Chem Catalysis* **2022**, *2* (6), 1362-1379. DOI: 10.1016/j.checat.2022.03.009.

[35] Jiang, Z.; Klyukin, K.; Alexandrov, V. First-principles study of adsorption–desorption kinetics of aqueous V2+/V3+ redox species on graphite in a vanadium redox flow battery. *Physical Chemistry Chemical Physics* **2017**, *19* (23), 14897-14901. DOI: 10.1039/C7CP02350B.

[36] Xu, A.; Shi, L.; Zeng, L.; Zhao, T. S. First-principle investigations of nitrogen-, boron-, phosphorus-doped graphite electrodes for vanadium redox flow batteries. *Electrochimica Acta* **2019**, *300*, 389-395. DOI: 10.1016/j.electacta.2019.01.109.

[37] Hassan, A.; Haile, A. S.; Tzedakis, T.; Hansen, H. A.; de Silva, P. The Role of Oxygenic Groups and sp3 Carbon Hybridization in Activated Graphite Electrodes for Vanadium Redox Flow Batteries. *ChemSusChem* **2021**, *14* (18), 3945-3952. DOI: 10.1002/cssc.202100966.

[38] Kang, M. G.; Ahn, W.; Kang, J.; Song, S. A.; Kim, K.; Woo, J. Y.; Jeong, Y.-C.; Koo, B.; Jung, D. S.; Lim, S. N. Superior electrocatalytic negative electrode with tailored nitrogen functional group for vanadium redox flow battery. *Journal of Energy Chemistry* **2023**, *78*, 148-157. DOI: 10.1016/j.jechem.2022.11.022.

[39] Howard, J. D.; Assary, R. S.; Curtiss, L. A. Insights into the Interaction of Redox Active Organic Molecules and Solvents with the Pristine and Defective Graphene Surfaces from Density Functional Theory. *The Journal of Physical Chemistry C* **2020**, *124* (5), 2799-2805. DOI: 10.1021/acs.jpcc.9b10403.

[40] Yuk, S. F.; Lee, M.-S.; Akhade, S. A.; Nguyen, M.-T.; Glezakou, V.-A.; Rousseau, R. First-principle investigation on catalytic hydrogenation of benzaldehyde over Pt-group metals. *Catalysis Today* **2022**, *388-389*, 208-215. DOI: https://doi.org/10.1016/j.cattod.2020.07.039.

[41] Bramley, G. A.; Nguyen, M.-T.; Glezakou, V.-A.; Rousseau, R.; Skylaris, C.-K. Understanding Adsorption of Organics on Pt(111) in the Aqueous Phase: Insights from DFT Based Implicit Solvent and Statistical Thermodynamics Models. *Journal of Chemical Theory and Computation* **2022**, *18* (3), 1849-1861. DOI: 10.1021/acs.jctc.1c00894.

[42] Singh, N.; Campbell, C. T. A Simple Bond-Additivity Model Explains Large Decreases in Heats of Adsorption in Solvents Versus Gas Phase: A Case Study with Phenol on Pt(111) in Water. *ACS Catalysis* **2019**, *9* (9), 8116-8127. DOI: 10.1021/acscatal.9b01870.

[43] Potts, D. S.; Bregante, D. T.; Adams, J. S.; Torres, C.; Flaherty, D. W. Influence of solvent structure and hydrogen bonding on catalysis at solid–liquid interfaces. *Chemical Society Reviews* **2021**, *50* (22), 12308-12337, 10.1039/D1CS00539A. DOI: 10.1039/D1CS00539A.

[44] Mathew, K.; Sundararaman, R.; Letchworth-Weaver, K.; Arias, T. A.; Hennig, R. G. Implicit solvation model for density-functional study of nanocrystal surfaces and reaction pathways. *The Journal of Chemical Physics* **2014**, *140* (8), 084106. DOI: 10.1063/1.4865107.

[45] Mathew, K.; Kolluru, V. S. C.; Mula, S.; Steinmann, S. N.; Hennig, R. G. Implicit self-consistent electrolyte model in plane-wave density-functional theory. *The Journal of Chemical Physics* **2019**, *151* (23), 234101. DOI: 10.1063/1.5132354.

[46] Hori, Y.; Takahashi, I.; Koga, O.; Hoshi, N. Reduction of CO2 on Ag. *Journal of Molecular Catalysis A: Chemical* **2003**, *199* (1-2), 39-47. DOI: 10.1016/S0022-0728(97)00447-6.

[47] Gong, K.; Fang, Q.; Gu, S.; Li, S. F. Y.; Yan, Y. Nonaqueous redox-flow batteries: organic solvents, supporting electrolytes, and redox pairs. *Energy & Environmental Science* **2015**, *8* (12), 3515-3530. DOI: 10.1039/c5ee02341f.

[48] Kresse, G.; Hafner, J. Ab initio molecular dynamics for liquid metals. *Phys Rev B Condens Matter* **1993**, *47* (1), 558-561. DOI: 10.1103/physrevb.47.558.

[49] Kresse, G.; Hafner, J. Ab initio molecular-dynamics simulation of the liquid-metal-amorphous-semiconductor transition in germanium. *Phys Rev B Condens Matter* **1994**, *49* (20), 14251-14269. DOI: 10.1103/physrevb.49.1425.

[50] Kresse, G.; Furthmuller, J. Efficiency of Ab-Ititio Energy Calculations for Metals and Semiconductors Using a Plane-Wave Basis Set. *Computational Materials Science* **1996**, *6* (1), 15-50. DOI: 10.1016/0927-0256(96)00008-0.

[51] Kresse, G.; Furthmuller, J. Efficient iterative schemes for ab initio total-energy calculations using a plane-wave basis set. *Physical Review B* **1996**, *54* (16), 11169-11186. DOI: 10.1103/PhysRevB.54.11169.

[52] Perdew, J. P.; Burke, K.; Ernzerhof, M. Generalized Gradient Approximation Made Simple. *Physical Review Letters* **1996**, *77* (18), 3865-3868.

[53] Grimme, S.; Antony, J.; Ehrlich, S.; Krieg, H. A consistent and accurate ab initio parametrization of density functional dispersion correction (DFT-D) for the 94 elements H-Pu. *The Journal of Chemical Physics* **2010**, *132* (15), 154104. DOI: 10.1063/1.3382344.

[54] Kresse, G.; Joubert, D. From ultrasoft pseudopotentials to the projector augmented-wave method. *Physical Review B* **1999**, *59* (3), 1758. DOI: 10.1103/PhysRevB.59.1758.

[55] Monkhorst, H. J.; Pack, J. D. Special points for Brillouin-zone integrations. *Physical Review B* **1976**, *13* (12), 5188-5192. DOI: 10.1103/PhysRevB.13.5188.

[56] Saeys, M.; Reyniers, M.-F.; Marin, G. B.; Neurock, M. Density Functional Study of Benzene Adsorption on Pt(111). *The Journal of Physical Chemistry B* **2002**, *106* (30), 7489-7498. DOI: 10.1021/jp0201231.

[57] Momma, K.; Izumi, F. VESTA 3 for three-dimensional visualization of crystal, volumetric and morphology data. *Journal of Applied Crystallography* **2011**, *44* (6), 1272-1276. DOI: 10.1107/S0021889811038970.

[58] Yu, M.; Trinkle, D. R. Accurate and efficient algorithm for Bader charge integration. *The Journal of Chemical Physics* **2011**, *134* (6), 064111. DOI: 10.1063/1.3553716.

[59] Henkelman, G.; Arnaldsson, A.; Jónsson, H. A fast and robust algorithm for Bader decomposition of charge density. *Computational Materials Science* **2006**, *36* (3), 354-360. DOI: 10.1016/j.commatsci.2005.04.010.

[60] Sanville, E.; Kenny, S. D.; Smith, R.; Henkelman, G. Improved grid-based algorithm for Bader charge allocation. *Journal of Computational Chemistry* **2007**, *28* (5), 899-908, https://doi.org/10.1002/jcc.20575. DOI: 10.1002/jcc.20575.

[61] Tang, W.; Sanville, E.; Henkelman, G. A grid-based Bader analysis algorithm without lattice bias. *Journal of Physics: Condensed Matter* **2009**, *21* (8), 084204. DOI: 10.1088/0953-8984/21/8/084204.

[62] Stukowski, A. Visualization and analysis of atomistic simulation data with OVITO–the Open Visualization Tool. *Modelling and Simulation in Materials Science and Engineering* **2010**, *18* (1), 015012. DOI: 10.1088/0965-0393/18/1/015012.

[63] Wang, V.; Xu, N.; Liu, J.-C.; Tang, G.; Geng, W.-T. VASPKIT: A user-friendly interface facilitating high-throughput computing and analysis using VASP code. *Computer Physics Communications* **2021**, *267*, 108033. DOI: 10.1016/j.cpc.2021.108033.

[64]. Bal, K. M.; Neyts, E. C. Modelling molecular adsorption on charged or polarized surfaces: a critical flaw in common approaches. Physical Chemistry Chemical Physics 2018, 20 (13), 8456-8459, 10.1039/C7CP08209F. DOI: 10.1039/C7CP08209F.

[65] Mason, S. E.; Sokol, E. A.; Cooper, V. R.; Rappe, A. M. Spontaneous Formation of Dipolar Metal Nanoclusters. *The Journal of Physical Chemistry A* **2009**, *113* (16), 4134-4137. DOI: 10.1021/jp8105088.

[66] Hoffmann, R. A chemical and theoretical way to look at bonding on surfaces. *Reviews of Modern Physics* **1988**, *60* (3), 601-628. DOI: 10.1103/RevModPhys.60.601.

[67] Filhol, J.-S.; Neurock, M. Elucidation of the Electrochemical Activation of Water over Pd by First Principles. *Angewandte Chemie International Edition* **2006**, *45* (3), 402-406. DOI: 10.1002/anie.200502540.

[68] Schwarz, K.; Sundararaman, R. The electrochemical interface in first-principles calculations. *Surface Science Reports* **2020**, *75* (2), 100492. DOI:10.1016/j.surfrep.2020.100492.